Research Square

Preprints are preliminary reports that have not undergone peer review.
They should not be considered conclusive, used to inform clinical practice,
or referenced by the media as validated information.

Order selection rules and interband geometry in dissipative nonlinear transport

yue fang

yue.fang@aalto.fi

Aalto University

Zhipei Sun

Aalto University

Article

Keywords:

Posted Date: November 5th, 2026

DOI: https://doi.org/10.21203/rs.3.rs-11305269/v1

License: This work is licensed under a Creative Commons Attribution 4.0 International License.
Read Full License

Additional Declarations: No competing interests reported.

Order selection rules and interband geometry in dissipative nonlinear transport

Rate-independent nonlinear transport probes quantum geometry, although its coefficients can also contain contributions determined solely by the dispersion and depend on the dissipative steady state. Here we establish a parity selection structure across response orders in a controlled open system: a Bloch Hamiltonian coupled to a uniform wide-band fermionic bath. Taking the dc limit before weak coupling at fixed positive temperature, we prove that the rate-independent coefficient, or finite part, vanishes at every odd order for a smooth periodic scalar band, irrespective of spatial symmetry, whereas finite terms remain allowed at even orders. Closed interband paths can supply the phase absent from scalar vertices and lift this restriction. For separated bands, a nonzero finite part at odd orders therefore requires virtual interband processes, even when only one band crosses the chemical potential. We derive the full transverse third-order finite part for two bands in closed form. In a tilted Chern model, competing geometric terms reverse the sign of the curvature–metric contribution alone, while comparison with two relaxation-time prescriptions resolves the dependence on the description of the steady state. Within the same bath model, subleading longitudinal terms combine with nonlinear poles to shift the asymptotic conductivity scaling intercept away from the microscopic finite part. The resulting framework connects a selection rule and its interband mechanism to the calculation and extraction of rate-independent nonlinear transport.

Introduction

Nonlinear Hall effects reveal how the geometry of Bloch wavefunctions shapes charge transport, including in systems whose symmetries forbid a linear Hall response [1]. At second order, a Berry curvature dipole produces a Hall current in conductors that preserve time reversal but break inversion symmetry [2–4]. A quantum metric dipole generates a second-order Hall current in $\mathcal{PT}$-symmetric antiferromagnets [5–7]. These responses make electrical transport sensitive to the structure of electronic states in momentum space beyond the information contained in the linear Hall conductivity.

Third-order Hall signals have also been observed [8, 9]. Their proposed geometric mechanisms include Berry curvature quadrupoles [10, 11], Berry connection polarizability [12, 13], and second-order field-induced Berry curvature [14]. Quantum metric quadrupoles also contribute to third-order transport [15–18]. The coexistence of these contributions makes their identification a central part of interpreting nonlinear signals. Their different powers of the relaxation time τ offer a useful distinction; in particular, the τ^0 term is conventionally called intrinsic and associated with band geometry [19, 20].

Rate independence alone, however, does not establish a geometric origin. Self-energy calculations and exact treatments of a fermionic bath show that dissipation changes geometric weights and occupations of the steady state [21, 22]. The preparation of the steady state and its relaxation dynamics thus enter the definition of an intrinsic current [23, 24].

The second-order bath response contains a finite term determined solely by the dispersion [22], while third-order geometric weights depend on the relaxation prescription [15]. These observations raise a question about the structure of the response: can its order determine when an origin in the dispersion alone is excluded? A selection rule across orders would identify when interband processes are necessary before their individual geometric contributions are resolved.

Here we establish an even–odd selection structure for a uniform wide-band fermionic bath, taking the dc limit before weak coupling at fixed positive temperature. A smooth periodic scalar band has no odd-order finite part, regardless of spatial symmetry, whereas even-order finite parts remain allowed. This distinction follows from a phase constraint: scalar vertices are real, while closed interband paths can supply the imaginary component needed for a real odd-order finite part. For separated bands, a nonzero odd-order finite part therefore requires virtual interband processes, including when only one band crosses the chemical potential.

We make this mechanism quantitative with an expression in closed form for the full two-band transverse third-order finite part. Its geometric terms can compete strongly enough to change the sign predicted by the curvature–metric contribution alone. We then connect this microscopic coefficient to the conductivity scaling intercept: within the same bath model, subleading longitudinal terms mix with nonlinear poles and shift the intercept even as the broadening vanishes. The selection rule, its interband mechanism, and this asymptotic relation provide a common basis for identifying, calculating, and extracting the finite part. Applying the intercept relation to disorder-controlled measurements requires a microscopic correspondence between the scattering mechanism and the bath description.

Results

An order selection rule for the dc finite part

We begin with a microscopic steady state in which the role of dissipation is fixed. Consider a Bloch Hamiltonian $h_0(\boldsymbol{k})$ coupled to a fermionic bath that produces the same momentum-independent broadening in every orbital [21, 22, 25]. All orbital positions are taken at the cell origin. The field enters through $h_A(\boldsymbol{k}) = h_0(\boldsymbol{k} - \boldsymbol{A})$, with $e = \hbar = 1$ and $\boldsymbol{E}(\omega) = \mathrm{i}\omega\boldsymbol{A}(\omega)$ (Supplementary Information, Sec. I). For a bath in thermal equilibrium, the self-energies and propagators are

$$\begin{aligned} \Sigma^{R/A} &= \mp \mathrm{i}\Gamma \mathbb{1}, \qquad \Sigma_s^{<}(\nu) = 2\mathrm{i}\Gamma f_0(\nu + s)\mathbb{1}, \\ G^{R/A}(z) &= [z - h_0 \pm \mathrm{i}\Gamma]^{-1}. \end{aligned} \tag{1}$$

Here f_0 is the Fermi function, and s is the external frequency shift at an insertion of the lesser self-energy. Although the retarded and advanced widths are energy independent, the lesser self-energy retains the full energy dependence of f_0. The zero-field occupations are therefore spectrally broadened (Supplementary Information, Sec. II.A). This occupation structure is essential to the finite part. Structured reservoirs require the extensions discussed in Supplementary Information, Sec. V.C.

Expanding the Peierls coupling generates vertices linear in the vector potential and

contact vertices containing two or more field factors. Keeping all of them makes a static uniform vector potential a pure momentum shift [26–29], which renders the dc response regular at finite Γ (Supplementary Information, Secs. I and II). We integrate over bath energy and the Brillouin zone before taking the dc limit and expand the symmetric order-n kernel $\Xi_n(0;\Gamma)$ at fixed $T > 0$. We call the Γ^0 coefficient the finite part (FP). It remains a well-defined expansion coefficient even when the conductivity diverges in the clean limit:

$$\sigma^{(n),[0]} = \mathrm{FP}_{\Gamma\to 0}\,\Xi_n(0;\Gamma), \qquad \bar{\sigma}_n = \Xi_n/n!, \tag{2}$$

where $\bar{\sigma}_n$ multiplies E^n in the current; at third order, $j^a = \sigma^{(3)}_{abcd}E_bE_cE_d/3!$. Matching the Drude terms of the scalar band to Boltzmann theory gives $\tau = 1/(2\Gamma)$, so the finite part is what a τ expansion calls the τ^0 term (Supplementary Information, Secs. I and II).

For a scalar band, $h_0(\boldsymbol{k}) = \varepsilon(\boldsymbol{k})$ has no internal orbital degrees of freedom. For any smooth periodic ε, its finite part obeys the order selection rule

$$\sigma^{(n),[0],\mathrm{sb}} = 0 \ \ (n \ \mathrm{odd}), \qquad \sigma^{(2),[0]} \not\equiv 0. \tag{3}$$

Here "sb" denotes a single scalar band. Equation (3) excludes an origin in the dispersion alone for a nonzero odd-order finite part without requiring spatial symmetry. Divergent odd-order terms, including the Drude pole, remain. The condition of fixed $T > 0$ is essential: the limit at zero temperature can fail to commute with weak coupling at critical fillings (Supplementary Information, Sec. V.D).

The selection rule follows from the phase needed to produce a real dc current. At order n, conversion from vector potentials to electric fields contributes i^{-n}, which is imaginary for odd n and real for even n. Frequency differentiation separates each closed response path w into a bath energy moment M_w and a vertex product τ_w; its contribution to the finite part is proportional to $\mathrm{i}^{-n}M_w\tau_w$. After rescaling the energy about the scalar-band pole as $\nu = \varepsilon + \Gamma x$, reflection $x \to -x$ maps the integrand defining the finite part to its complex conjugate. The moment M_w is therefore real (Supplementary Information, Secs. III.A and IV.B).

A scalar Hamiltonian has no internal orbital states to mix. Every vertex is a real derivative of the same dispersion, so its product τ_w, distinct from the relaxation time, is real as well [Fig. 1(b)]. The scalar vertices therefore cannot supply an additional imaginary factor. At odd order the finite-part contributions are purely imaginary, whereas the dc response and its Laurent coefficients must be real; their sum of finite parts is consequently zero. At even order no such phase obstruction remains. Changing the shape or spatial symmetry of a scalar dispersion does not change this phase counting.

At second order, the residues in the direct sector cancel and the finite contribution comes from contact vertices (Supplementary Information, Sec. III.B); integration by parts over the periodic Brillouin zone gives

$$\sigma^{(2),[0]}_{abc} = \frac{1}{24}\int_{\mathrm{BZ}} \frac{\mathrm{d}^d k}{(2\pi)^d} v_a v_b v_c f_0^{(4)}(\varepsilon), \qquad v_a = \partial_a\varepsilon. \tag{4}$$

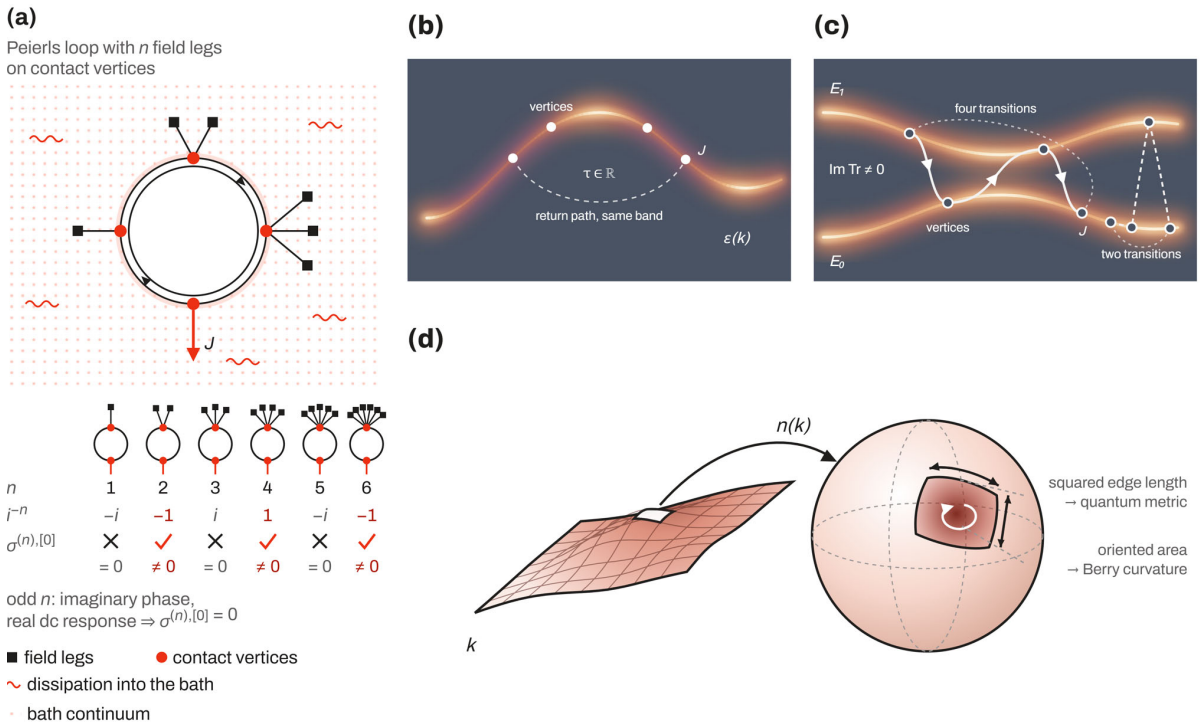


Figure 1

Here $j^a = \frac{1}{2}\sigma^{(2)}_{abc}E_bE_c$. This term depends only on the band dispersion [22], whereas a relaxation-time model of a scalar band contains only a rate pole at each order [30]. Thus even-order finite terms depend on the description of the steady state, whereas the bath phase constraint excludes their odd-order counterparts. An allowed even-order contribution can still integrate to zero for particular dispersions or symmetries. Figure 1(a) illustrates the phase pattern through $n = 6$; Supplementary Information, Sec. III, gives the proof at all orders and explicit checks.

Interband geometry in the third-order response

With multiple bands, current and field vertices connect distinct internal states. Products of their matrix elements around a closed path can be complex even though every vertex is Hermitian. The eigenstate phase choices cancel around the loop, so this complex structure is independent of those choices. Its imaginary component supplies the additional factor needed for a real odd-order finite part. This is how interband structure can lift the restriction for a scalar band. To identify the contributing paths, we resolve the propagator into band projectors:

$$h_0 = \sum_n E_n P_n, \qquad G^{R/A}(z) = \sum_n \frac{P_n}{z - E_n \pm \mathrm{i}\Gamma}. \tag{5}$$

Each path contains a closed trace $\mathrm{Tr}[P\,V\,P\cdots J]$, and the phase constraint selects its imaginary component at odd order and its real component at even order. Interband transitions thus permit a nonzero odd-order finite part, but symmetry or cancellation can still make it vanish.

To isolate interband effects, we subtract from the full response the sum of independent scalar-band responses with the same dispersions $E_n(\boldsymbol{k})$; the difference is R. For non-

degenerate bands separated throughout the Brillouin zone, these dispersions are smooth and periodic. Each scalar reference then has zero odd-order finite part. The full response therefore satisfies

$$\sigma^{(n),[0]} = \mathrm{FP}\, R \qquad (n \text{ odd}). \tag{6}$$

Equation (6) establishes the need for virtual interband transitions whenever the odd-order finite part is nonzero. This distinction matters even with a single band at the chemical potential: an isolated band within a multiorbital system retains virtual transitions that a scalar dispersion does not.

We evaluate the full transverse third-order component $\sigma^{(3)}_{yxxx}$ for two bands. This component includes both Hall and Ohmic contributions; their separation requires permutations of the current index with the field indices. A closed two-band path has an even number of band changes and, at third order, at most four vertices. It therefore makes zero, two, or four transitions. The zero-transition traces are real and give no finite part. Hence $\mathrm{FP}\, R = \mathrm{FP}(\mathsf{T}_2 + \mathsf{T}_4)$, where T_2 and T_4 contain two and four transitions, respectively [Fig. 1(c)]. The corresponding decomposition at finite Γ is given in the Supplementary Information (Sec. IV.A).

Only imaginary trace components survive in the third-order finite part, which makes it a polar tensor odd under time reversal. Time reversal symmetry makes its density in momentum space odd, so the Brillouin zone integral vanishes. For the nondegenerate bands considered here, a $\mathcal{PT}$-type symmetry instead forces the density to vanish at each momentum (Supplementary Information, Sec. V.A).

The surviving traces with two or four transitions can be expressed in terms of band geometry. For $h = d_0\sigma_0 + \boldsymbol{d}\cdot\boldsymbol{\sigma}$, set $r = |\boldsymbol{d}|$, $\boldsymbol{n} = \boldsymbol{d}/r$, and $\Delta = 2r$. The map $\boldsymbol{n}(\boldsymbol{k})$ sends momentum space to the Bloch sphere, where squared lengths encode the quantum metric and oriented areas encode the Berry curvature [Fig. 1(d)]. For the lower band, define $\Omega^{yx} = \boldsymbol{n}\cdot(\partial_x\boldsymbol{n}\times\partial_y\boldsymbol{n})/2$ and $g^{xx} = \{|\partial_x\boldsymbol{d}|^2 - (\boldsymbol{n}\cdot\partial_x\boldsymbol{d})^2\}/\Delta^2$. The path that alternates between P_0 and P_1 then gives

$$\mathrm{Im}\ \mathrm{Tr}[P_0V_xP_1V_xP_0V_xP_1J_y] = 8r^4\,\Omega^{yx}g^{xx}. \tag{7}$$

This path generates the curvature–metric product. The remaining paths generate terms involving gap gradients and interband derivatives. Their weights follow from the bath energy residue expansion in Supplementary Information, Sec. IV.B. At fixed $T > 0$ and nonzero direct gap, the exact result is

$$\begin{aligned} r^{[0]}_{yxxx}(\boldsymbol{k}) &= \bar{f}\, g_{\mathrm{sea}} + \sum_{s=0,1}\sum_{q=1}^{3} f_0^{(q)}(E_s)\, g_{s,q}, \\ \sigma^{(3),[0]}_{yxxx} &= \int_{\mathrm{BZ}} \frac{\mathrm{d}^d k}{(2\pi)^d}\, r^{[0]}_{yxxx}(\boldsymbol{k}), \end{aligned} \tag{8}$$

where $E_{0,1} = d_0 \mp r$ and $\bar{f} = f_0(E_0) - f_0(E_1)$. The indices s and q label the band and the order of differentiation with respect to energy. The occupation difference weights the Fermi sea term. Derivatives of f_0 weight the terms concentrated near the chemical potential,

making the geometric response sensitive to filling and temperature.

The coefficient of the first derivative illustrates why several geometric terms must be retained. With $\Omega = 2r^2\Omega^{yx}$, $\mathcal{G} = 4r^2 g^{xx}$, and $A = \boldsymbol{n} \cdot (\partial_x \boldsymbol{d} \times \partial_x^2 \boldsymbol{d})$, its weight for the lower band is

$$g_{0,1} = \frac{3\Omega\mathcal{G}}{8r^5} + \frac{3A\, v_-^y}{4r^4}, \qquad v_-^y = \partial_y E_0. \tag{9}$$

The term containing A depends on $\partial_x^2 \boldsymbol{d}$ and is not captured by the curvature–metric product. The remaining weights involve covariant interband derivatives [15, 31], gap gradients, and band-diagonal Hamiltonian derivatives. All weights admit trace expressions invariant under eigenstate phase changes. Integration by parts can redistribute them among geometric groups while preserving their sum. Supplementary Information, Sec. IV.D, gives the complete expressions and separates this freedom from a physical change of orbital embedding, which changes the current and contact vertices.

We evaluate equation (8) for a tilted Chern model of the Qi–Wu–Zhang type [32],

$$\begin{aligned} h/t &= d_0\sigma_0 + \sin k_x \sigma_x + \sin k_y \sigma_y \\ &\quad + (m - \cos k_x - \cos k_y)\sigma_z, \\ d_0 &= \lambda_1 \sin k_x + \lambda_2 \sin(k_x + k_y), \end{aligned} \tag{10}$$

with $(m, \lambda_1, \lambda_2) = (1.2, 0.5, 0.35)$. Energies are measured in hopping units t and momenta in units of the inverse lattice constant; the minimum direct gap is $1.6t$. Without the tilt, an antiunitary mirror forbids the $xxxx$ third-order finite part but allows $yxxx$; the scalar tilt breaks this symmetry and permits a longitudinal finite part. Topologically trivial variants also give a nonzero remainder (Supplementary Information, Sec. V.A), so a nonzero Chern number is not required. This model allows us to check equation (8) against the finite-rate kernel and to compare the curvature–metric contribution with the complete response.

In Fig. 2(a), the bath response has a minimum near $\mu = -1.4t$ at $T = 0.1t$, close to the lower-band saddle energy $-1.38t$, consistent with the filling sensitivity of the Fermi derivative terms in equation (8). At $\mu = -t$, the temperature dependence is nonmonotonic [Fig. 2(b)]. Extrapolations of the finite-Γ kernel follow both trends (Supplementary Information, Sec. VI.A).

Figure 2(a) also compares the bath with two relaxation-time prescriptions. Their different third-order geometric weights were established in quantum kinetic theory by comparing a rate N/τ at response order N with a uniform rate $1/\tau$ [15, Sec. VIII]. We evaluate these two prescriptions alongside the exact bath result [13, 33, 34], holding the Hamiltonian, electromagnetic coupling, temperature, and chemical potential fixed. At $\mu = -t$ and $T = 0.1t$, the finite parts are 0.109 for the bath, 0.177 for N/τ, and 0.055 for the uniform rate, in symmetric kernel units (Supplementary Information, Sec. VI.B), and their filling dependence differs in shape and sign [Fig. 2(a)]. The microscopic bath supplies the spectrally broadened occupations specified by equation (1), whereas the two relaxation-time models relax toward $f_0(h)$. These differences occur at fixed band geometry: the bath determines both the occupations and the relaxation dynamics, while the two recursions impose different rates on a common target density matrix.

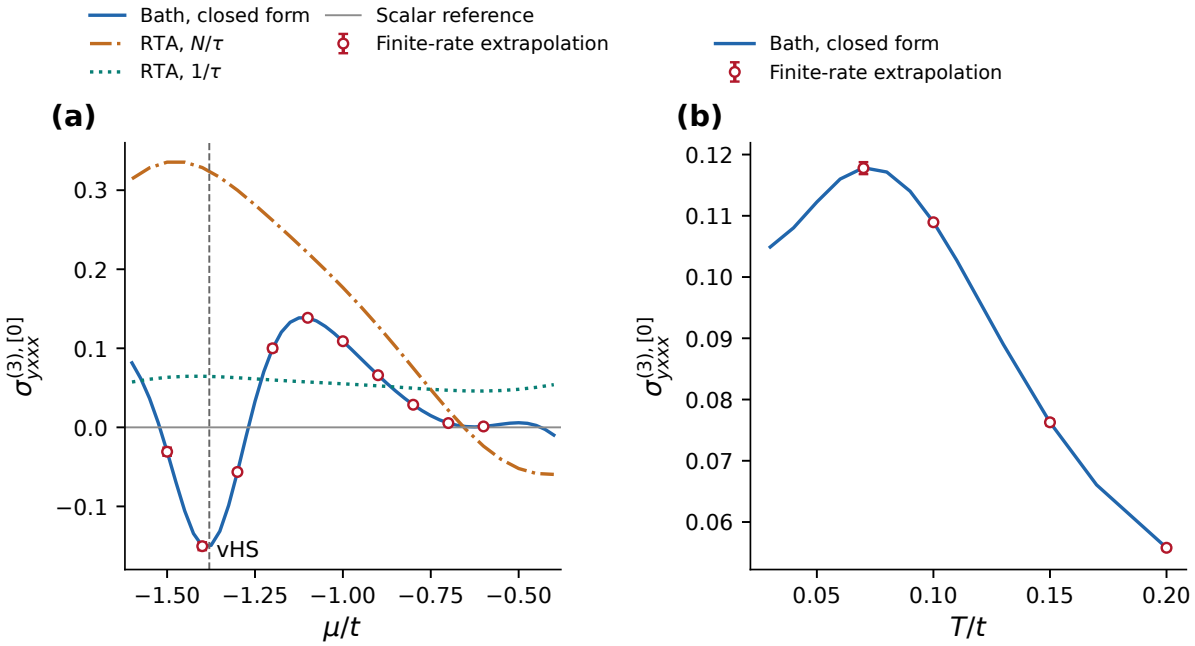


Figure 2

We next resolve the bath result into geometric contributions [Fig. 3]. Their competition changes the sign relative to the curvature–metric contribution alone: at $\mu = -t$ and $T = 0.1t$, that group contributes -0.187, whereas the full finite part is $+0.109$. The contribution from Berry curvature multiplied by the squared gap gradient is $+0.116$, and the remaining derivative terms contribute $+0.180$. The first and third groups largely cancel near the Fermi contour. The group involving the squared gap gradient is weaker pointwise but extends over a broader momentum region. The numerical group weights refer to the decomposition in Supplementary Information, Sec. IV.D; their sum is independent of this choice. A complementary decomposition by interband paths also shows substantial cancellation between the two- and four-transition sectors (Supplementary Fig. S1).

The Fermi sea term in equation (8) does not imply a finite third-order response in the insulator at zero temperature. For two-band $yxxx$, its coefficient is a total divergence, $g_{\mathrm{sea}} = \partial_x W_x + \partial_y W_y$, with $\boldsymbol{W}$ smooth, periodic, and gauge invariant whenever the direct gap is nonzero. Integration by parts turns the sea term into the Fermi surface integral $-\int_{\mathrm{BZ}} \frac{\mathrm{d}^d k}{(2\pi)^d} \boldsymbol{W} \cdot \nabla_{\boldsymbol{k}} \bar{f}$, which vanishes with the explicit Fermi surface terms as $T \to 0$ when the chemical potential lies in the global gap (Supplementary Information, Secs. IV.D and V.B). The two-band $yxxx$ finite part therefore vanishes in this insulating limit, with $T \to 0$ taken after the expansion at weak coupling.

Conductivity scaling and the microscopic finite part

To extract a rate-independent nonlinear coefficient, scaling analyses often use the longitudinal conductivity as a measure of relaxation: if it is proportional to the relaxation time, the constant coefficient of a third-order scaling polynomial identifies the microscopic finite part [15, Sec. VII]. Theories that resolve individual mechanisms go further: disorder can also contribute to the constant, and the full set of scaling coefficients, together with symmetry, helps identify the contributing processes [35–37]. These analyses build on microscopic

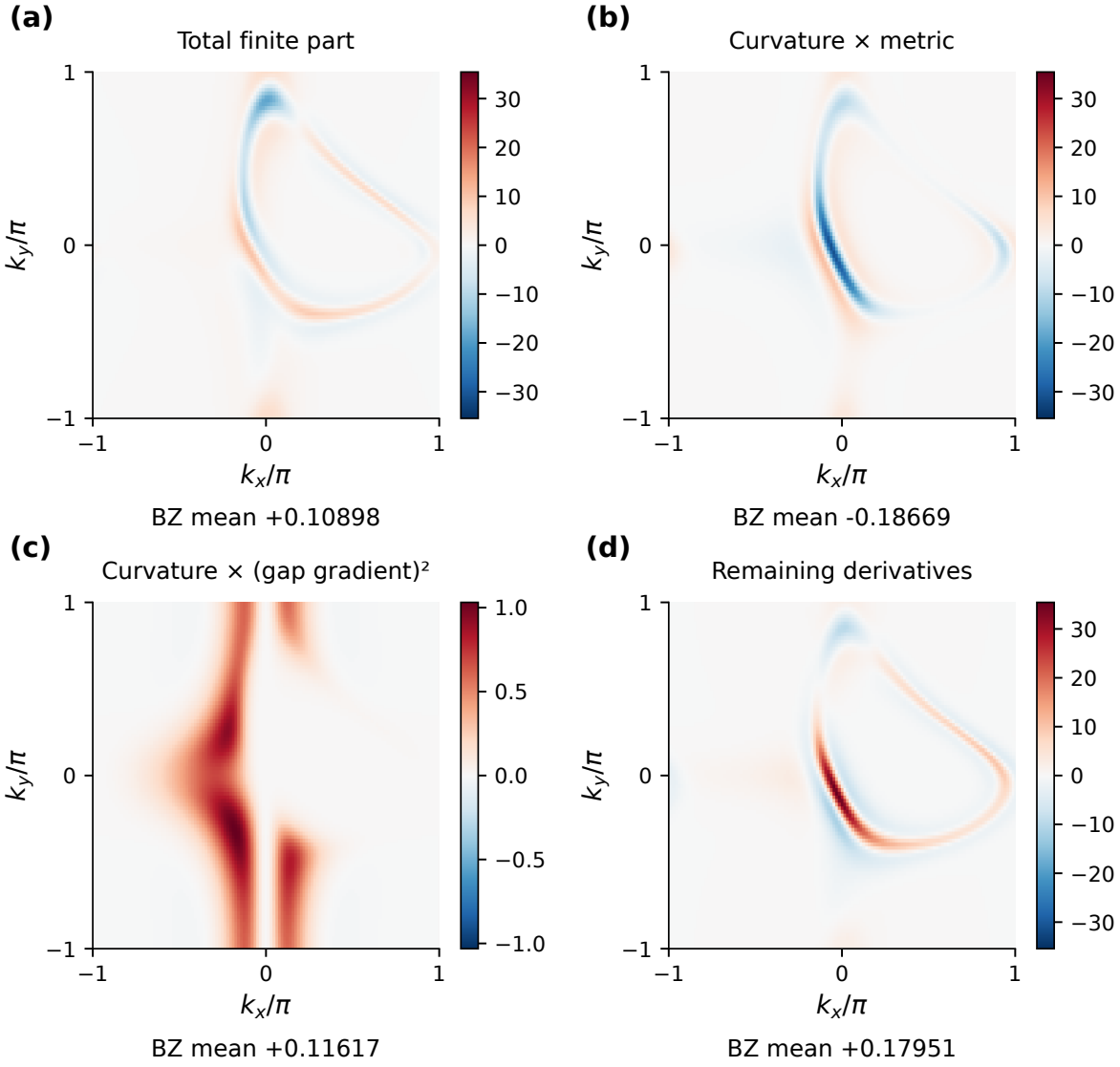

(a)
Total finite part
BZ mean +0.10898
(b)
Curvature × metric
BZ mean -0.18669
(c)
Curvature × (gap gradient)²
BZ mean +0.11617
(d)
Remaining derivatives
BZ mean +0.17951
k_x/π
k_y/π

Figure 3

descriptions of disorder-related nonlinear transport [38–40].

A further shift arises even within a fixed relaxation model when the longitudinal conductivity departs from exact inverse-rate scaling. Although its subleading terms vanish at weak coupling, their products with divergent nonlinear terms can remain finite. We hold the Hamiltonian, electromagnetic coupling, temperature, and chemical potential fixed and vary only the common bath broadening Γ. For the present bath, write $\sigma_{xx} = D_x/\Gamma + b\Gamma + c\Gamma^2 + O(\Gamma^3)$ and $\Xi^y_{xxx} = A_3/\Gamma^3 + A_2/\Gamma^2 + A_1/\Gamma + \sigma^{(3),[0]}_{yxxx} + O(\Gamma)$. For $D_x \neq 0$, eliminating Γ in favor of σ_{xx} feeds the divergent third-order terms into the constant coefficient of the large-σ_{xx} expansion, in the regime where both expansions hold:

$$C_0^{(\sigma)} = \sigma^{(3),[0]}_{yxxx} - \frac{2A_2 b + 3A_3 c}{D_x}. \tag{11}$$

Equation (11) separates the microscopic finite part from the contribution transferred into the intercept by the nonlinear poles. At $\mu = -t$, $T = 0.1t$, this gives $C_0^{(\sigma)} = 0.194$ instead of $\sigma^{(3),[0]}_{yxxx} = 0.109$, in symmetric kernel units [Fig. 4(b); Supplementary Information, Sec. VI.C]. Figure 4(a) verifies the required subleading longitudinal terms against the finite-rate Kubo bubble. In panel (b), subtracting the divergent rate terms or the positive powers of longitudinal conductivity gives different constants as $\Gamma \to 0$. The two limits remain distinct as the rate decreases. Recovering the microscopic finite part requires the longitudinal coefficients b and c together with the nonlinear pole coefficients of the same bath model. Equation (11) relates asymptotic coefficients of that model. Applying it to measurements with tunable disorder requires a microscopic correspondence between scattering and bath broadening, and a consistent derivation of the longitudinal and nonlinear coefficients for the relevant scattering mechanism.

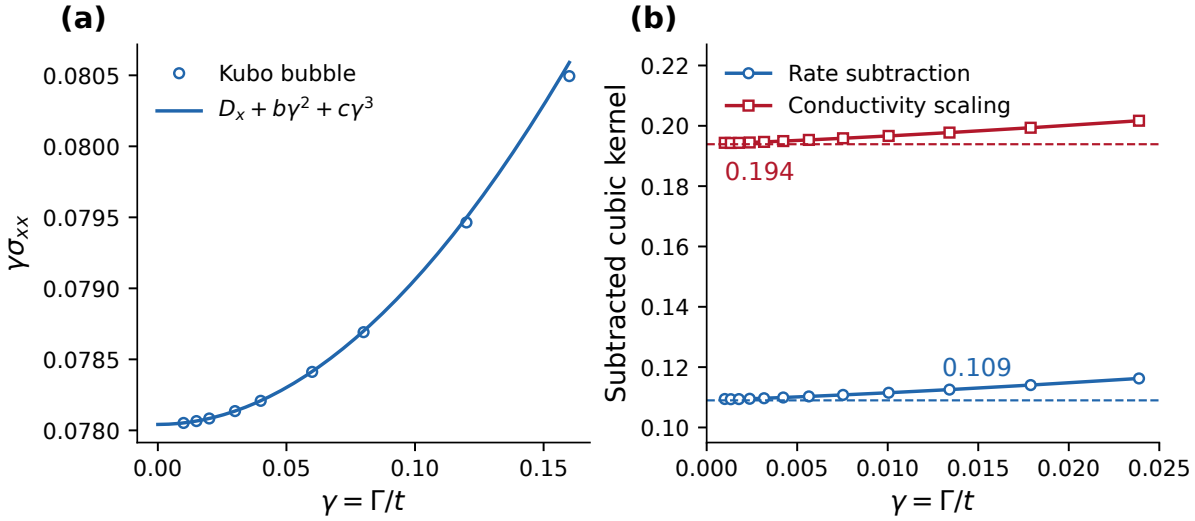


Figure 4

Discussion

The selection rule distinguishes information carried by band energies from information that requires interband processes. In the uniform wide-band bath, a smooth periodic scalar dispersion has no odd-order dc finite part when weak coupling follows the dc limit

at fixed $T > 0$. The term allowed at second order that depends solely on dispersion [22] therefore has no odd-order counterpart. For separated bands, this gives a criterion for assessing reduced models: reproducing the dispersion of the band at the chemical potential is insufficient if the target response has a nonzero odd-order finite part. The necessary virtual transitions involve the other bands even when those bands do not cross the chemical potential.

An interband origin does not specify a unique geometric contribution. Our exact two-band solution resolves the terms that must be combined for the bath response; their competition can change the sign predicted by the curvature–metric term alone. This result builds on established third-order geometric mechanisms and their sensitivity to relaxation prescriptions [14, 15]. The microscopic bath fixes the occupations and geometric weights together, providing a common reference for the two relaxation-time recursions. Their comparison makes clear why identical Bloch geometry need not imply identical rate-independent transport.

The scaling correction addresses how that coefficient is inferred. Theories that resolve individual mechanisms already identify disorder contributions to the constant term [36]. The additional shift in equation (11) arises within a fixed mechanism: a subleading longitudinal contribution can multiply a nonlinear divergence to leave a finite constant. The scalar Drude sector can therefore enter the scaling intercept even though its microscopic odd-order finite part is zero. A joint treatment of longitudinal and nonlinear transport is needed to distinguish these two statements. For impurity scattering, the corresponding calculation must include field-induced interband coherence [41] and multiphoton vertices generated by the self-energy [42] consistently (Supplementary Information, Sec. V.C).

The phase constraint also supplies symmetry tests. In the nondegenerate $\mathcal{PT}$-type systems treated here, the odd-order finite part vanishes at every momentum. Testing this prediction requires separating the microscopic coefficient from divergent terms and correcting any conductivity scaling intercept. Kramers-degenerate bands require an extension to degenerate subspaces, while higher odd-order Hall signals [43] motivate examining the criterion beyond third order. Measurements of current noise provide a complementary route to geometry through fluctuation-dissipation relations involving nonlinear optical responses [44].

The controlled bath model therefore links a selection rule across response orders to the interband processes that can lift it. The complete third-order expression makes those processes calculable, and its joint expansion with longitudinal transport distinguishes the microscopic finite part from the conductivity scaling intercept. This connection specifies both the origin of the surviving response and how its coefficient is inferred within the model.

Methods

Response calculation and extraction of the finite part

We use the equilibrium fermionic bath in equation (1), with the same broadening in every orbital and all orbital positions at the cell origin. The response contains every current and Peierls contact vertex at the required field order. Bath energy and momentum integrations precede the dc limit; the expansion at weak coupling is then taken at fixed $T > 0$. The

complete kernel, static-leg identity, and construction in terms of spectral paths are given in Supplementary Information, Secs. I–IV. All numerical results use $e = \hbar = t = a = 1$, where a is the lattice constant, and normalized Brillouin zone integrals are evaluated as means over uniform periodic grids. Third-order values are symmetric kernels, six times the coefficient of E_x^3 in the current.

For the model in equation (10), the filling and temperature scans use 128×96 momentum points, increased to 256×192 for $T < 0.07t$. At $\mu = -t$ and $T = 0.1t$, increasing the square grid from 96×96 to 384×384 changes the finite part evaluated in closed form by less than 10^{-9} in relative terms. At finite rates, integration over the bath energy uses Gauss–Legendre quadrature resolving the broadening around each band pole and the thermal scale near the chemical potential. Calculations below $\Gamma/t = 0.03$ use 40-digit arithmetic to control cancellation of large pole contributions. The geometric maps use the archived 128×96 samples without interpolation.

Writing $\gamma = \Gamma/t$, we fit the real finite-rate kernel to

$$Y(\gamma) = \sum_{p=-N}^{-1} a_p \gamma^p + \sigma^{(n),[0]} + \sum_{j=1}^{q} \left[b_j \gamma^j \ln \gamma + d_j \gamma^j \right]. \tag{12}$$

The reference fit uses $N = 4$, $q = 2$, rates $\gamma < 0.03$, and relative least squares. Extra negative powers and logarithms probe sensitivity to the fitting basis; the interband remainder itself has only γ^{-2} and γ^{-1} poles. The bars in Fig. 2 report the largest intercept change for $q \in \{1, 2, 3\}$ and three nested rate windows, obtained by dropping zero, one, or two of the largest retained rates at fixed $N = 4$. They measure fit sensitivity rather than statistical uncertainty. Fits including negative powers through $N = 5, 6$ provide a separate check of the pole basis. Supplementary Data 1 supplies the sampled rates, extrapolated values, and measures of fit stability.

A second check subtracts analytic pole coefficients evaluated on the same momentum grid and fits the residual with polynomials of degrees one to three over windows up to $\gamma = 0.03$. For 13 two-band parameter points, the extracted finite part agrees with the closed form within 3.1×10^{-5}. This checks the expansion against the finite-rate kernel; it is not an independent derivation of the analytic pole coefficients. A control using a scalar band with eigenvectors independent of momentum gives a third-order finite part of magnitude at most 1.1×10^{-4} over seven fillings. The control dispersion, exact residue identities, and validation curves are given in Supplementary Information, Secs. III and VI.

Relaxation-time and conductivity scaling comparisons

The two relaxation-time calculations use the same Hamiltonian and equilibrium target $\rho_0 = f_0(h)$, with the recursion in a fixed orbital basis

$$\mathrm{i}[h, \rho_N] + \frac{c_N}{\tau} \rho_N = -E_b \partial_b \rho_{N-1}, \qquad c_N = N \text{ or } 1. \tag{13}$$

The third-order current is obtained by integrating $\mathrm{Tr}[\rho_3 \partial_a h]$. For the uniform-rate prescription, the finite parts on 96×72 and 192×144 grids differ by less than 10^{-13} at $\mu = -t$ and $T = 0.1t$. Supplementary Information, Sec. VI.B, gives the expansion and normalization

used for both prescriptions.

For the scaling comparison, the finite-rate longitudinal Kubo response is evaluated with the same bath. Its coefficients at $\mu = -t$ and $T = 0.1t$ are $D_x = 0.0780$, $b = 0.106$, and $c = -0.0395$; the cubic pole coefficients are $A_2 = -0.0526$ and $A_3 = -0.03815$. Equation (11) then gives the rounded intercept 0.194, compared with the microscopic finite part 0.109. Supplementary Information, Sec. VI.C and Appendix B, provides the derivation, and Supplementary Data 1 contains the finite-rate values.

Data availability

The numerical source data for the main and supplementary figures, including the finite-rate data used for extrapolation and validation, are provided in Supplementary Data 1 as CSV files organized by figure and panel, with column definitions. Model parameters are specified in the corresponding figure captions.

Code availability

The custom code used to calculate the response functions and reproduce the numerical results is available from the corresponding author upon reasonable request.

Supplementary information

Supplementary Information provides the detailed derivations and additional numerical checks. Supplementary Data 1 contains numerical source data.

References

[1] Du, Z. Z., Lu, H.-Z. & Xie, X. C. Nonlinear Hall effects. *Nat. Rev. Phys.* **3**, 744–752 (2021).

[2] Sodemann, I. & Fu, L. Quantum nonlinear Hall effect induced by Berry curvature dipole in time-reversal invariant materials. *Phys. Rev. Lett.* **115**, 216806 (2015).

[3] Ma, Q. *et al.* Observation of the nonlinear Hall effect under time-reversal-symmetric conditions. *Nature* **565**, 337–342 (2019).

[4] Kang, K., Li, T., Sohn, E., Shan, J. & Mak, K. F. Nonlinear anomalous Hall effect in few-layer WTe_2. *Nat. Mater.* **18**, 324–328 (2019).

[5] Liu, H. *et al.* Intrinsic second-order anomalous Hall effect and its application in compensated antiferromagnets. *Phys. Rev. Lett.* **127**, 277202 (2021).

[6] Gao, A. *et al.* Quantum metric nonlinear Hall effect in a topological antiferromagnetic heterostructure. *Science* **381**, 181–186 (2023).

[7] Wang, N. *et al.* Quantum-metric-induced nonlinear transport in a topological antiferromagnet. *Nature* **621**, 487–492 (2023).

[8] Lai, S. *et al.* Third-order nonlinear Hall effect induced by the Berry-connection polarizability tensor. *Nat. Nanotechnol.* **16**, 869–873 (2021).

[9] He, P. *et al.* Third-order nonlinear Hall effect in a quantum Hall system. *Nat. Nanotechnol.* **19**, 1460–1465 (2024).

[10] Zhang, C.-P., Gao, X.-J., Xie, Y.-M., Po, H. C. & Law, K. T. Higher-order nonlinear anomalous Hall effects induced by Berry curvature multipoles. *Phys. Rev. B* **107**, 115142 (2023).

[11] Sankar, S. *et al.* Experimental evidence for a Berry curvature quadrupole in an antiferromagnet. *Phys. Rev. X* **14**, 021046 (2024).

[12] Gao, Y., Yang, S. A. & Niu, Q. Field induced positional shift of Bloch electrons and its dynamical implications. *Phys. Rev. Lett.* **112**, 166601 (2014).

[13] Liu, H. *et al.* Berry connection polarizability tensor and third-order Hall effect. *Phys. Rev. B* **105**, 045118 (2022).

[14] Xiang, L., Zhang, C., Wang, L. & Wang, J. Third-order intrinsic anomalous Hall effect with generalized semiclassical theory. *Phys. Rev. B* **107**, 075411 (2023).

[15] Mandal, D., Sarkar, S., Das, K. & Agarwal, A. Quantum geometry induced third-order nonlinear transport responses. *Phys. Rev. B* **110**, 195131 (2024).

[16] Li, H. *et al.* Quantum geometry quadrupole-induced third-order nonlinear transport in antiferromagnetic topological insulator $MnBi_2Te_4$. *Nat. Commun.* **15**, 7779 (2024).

[17] Liu, X.-Y. *et al.* Giant third-order nonlinearity induced by the quantum metric quadrupole in few-layer WTe_2. *Phys. Rev. Lett.* **134**, 026305 (2025).

[18] Yu, H. *et al.* Quantum metric third-order nonlinear Hall effect in a non-centrosymmetric ferromagnet. *Nat. Commun.* **16**, 7698 (2025).

[19] Holder, T., Kaplan, D. & Yan, B. Consequences of time-reversal-symmetry breaking in the light-matter interaction: Berry curvature, quantum metric, and diabatic motion. *Phys. Rev. Research* **2**, 033100 (2020).

[20] Kaplan, D., Holder, T. & Yan, B. Unification of nonlinear anomalous Hall effect and nonreciprocal magnetoresistance in metals by the quantum geometry. *Phys. Rev. Lett.* **132**, 026301 (2024).

[21] Michishita, Y. & Nagaosa, N. Dissipation and geometry in nonlinear quantum transports of multiband electronic systems. *Phys. Rev. B* **106**, 125114 (2022).

[22] Guo, Z., Liu, X.-Y., Wang, H., Shi, L.-k. & Chang, K. Dissipation-shaped quantum geometry in nonlinear transport. *Phys. Rev. Lett.* **136**, 206303 (2026).

[23] Xiao, C., Cao, J., Niu, Q. & Yang, S. A. Proper definition of intrinsic nonlinear current. *Phys. Rev. Lett.* **135**, 256306 (2025).

[24] Terada, I., Kitamura, S., Watanabe, H. & Ikeda, H. Problem of nonlinear conductivity within relaxation time approximation in noncentrosymmetric insulators. *Phys. Status Solidi B* **262**, 2400533 (2025).

[25] Matsyshyn, O., Song, J. C. W., Sodemann Villadiego, I. & Shi, L.-k. Fermi–Dirac staircase occupation of Floquet bands and current rectification inside the optical gap of metals: An exact approach. *Phys. Rev. B* **107**, 195135 (2023).

[26] Aversa, C. & Sipe, J. E. Nonlinear optical susceptibilities of semiconductors: Results with a length-gauge analysis. *Phys. Rev. B* **52**, 14636–14645 (1995).

[27] Ventura, G. B., Passos, D. J., Lopes dos Santos, J. M. B., Viana Parente Lopes, J. M. & Peres, N. M. R. Gauge covariances and nonlinear optical responses. *Phys. Rev. B* **96**, 035431 (2017).

[28] Parker, D. E., Morimoto, T., Orenstein, J. & Moore, J. E. Diagrammatic approach to nonlinear optical response with application to Weyl semimetals. *Phys. Rev. B* **99**, 045121 (2019).

[29] Ahmad, S. & Xue, F. Length–velocity gauge equivalence of quantum geometric nonlinear conductivity in the adiabatic dc limit. *Phys. Rev. B* (2026). URL https://doi.org/10.1103/r23j-t8kt. Accepted 14 September 2026.

[30] Pinho, J. M. A., Amorim, B., Bludov, Y. V. & Viana Parente Lopes, J. M. Exact nonlinear dynamics of single band metallic systems with dissipation: From optical to dc currents. *Phys. Rev. B* **113**, 224309 (2026).

[31] Ahn, J., Guo, G.-Y., Nagaosa, N. & Vishwanath, A. Riemannian geometry of resonant optical responses. *Nat. Phys.* **18**, 290–295 (2022).

[32] Qi, X.-L., Wu, Y.-S. & Zhang, S.-C. Topological quantization of the spin Hall effect in two-dimensional paramagnetic semiconductors. *Phys. Rev. B* **74**, 085308 (2006).

[33] Farrag, S., Mele, E. J. & Low, T. High order geometric channels for nonlinear transport in Bloch bands. Preprint at arXiv (2026). URL https://arxiv.org/abs/2607.20702.

[34] Das, K., Lahiri, S., Atencia, R. B., Culcer, D. & Agarwal, A. Intrinsic nonlinear conductivities induced by the quantum metric. *Phys. Rev. B* **108**, L201405 (2023).

[35] Gong, Z.-H., Du, Z. Z., Sun, H.-P., Lu, H.-Z. & Xie, X. C. Scaling analysis of quantum geometry in second-order nonlinear transport. *Sci. Bull.* **71**, 4422–4428 (2026).

[36] Gong, Z.-H., Wei, Z.-H., Lu, H.-Z. & Xie, X. C. Identifying geometric third-order nonlinear transport in disordered materials. *Phys. Rev. X* **16**, 031012 (2026).

[37] Chu, R. Y. *et al.* Third-order nonlinear Hall effect in altermagnet RuO_2. *Phys. Rev. Lett.* **135**, 216703 (2025).

[38] Du, Z. Z., Wang, C. M., Li, S., Lu, H.-Z. & Xie, X. C. Disorder-induced nonlinear Hall effect with time-reversal symmetry. *Nat. Commun.* **10**, 3047 (2019).

[39] Du, Z. Z., Wang, C. M., Sun, H.-P., Lu, H.-Z. & Xie, X. C. Quantum theory of the nonlinear Hall effect. *Nat. Commun.* **12**, 5038 (2021).

[40] Barman, C. K., Chattopadhyay, A., Sarkar, S., Zhu, J.-X. & Nandy, S. Role of disorder in the third-order anomalous Hall effect in time-reversal symmetric systems. *Phys. Rev. B* **111**, 235113 (2025).

[41] Xiao, C., Du, Z. Z. & Niu, Q. Theory of nonlinear Hall effects: Modified semiclassics from quantum kinetics. *Phys. Rev. B* **100**, 165422 (2019).

[42] Rostami, H. & Cappelluti, E. Dominant role of two-photon vertex in nonlinear response in two-dimensional Dirac systems. *npj 2D Mater. Appl.* **5**, 50 (2021).

[43] Li, X. *et al.* Higher odd-order nonlinear Hall effect in magnetic topological insulator $Mn(Bi_{1-x}Sb_x)_2Te_4$. *Nat. Commun.* **17**, 6652 (2026).

[44] Wang, R. *et al.* Quantum geometric fluctuation-dissipation relation for nonlinear transport. *Phys. Rev. Lett.* **137**, 026301 (2026).

Figure legends

Figure 1. Order selection and its interband geometric origin. The response is evaluated for a uniform wide-band bath, with dc taken before weak coupling at fixed $T > 0$. (a) Peierls response loops contain field legs (squares), contact vertices (red dots), and a current vertex J; red wavy arrows denote coupling to the bath. With a real bath moment and a real scalar vertex product, the phase i^{-n} forces every odd-order finite part to vanish. The even-order check marks and $\neq 0$ symbols indicate that a finite part is allowed; its value depends on the dispersion. (b) A closed scalar-band path has a real vertex product. (c) Two- and four-transition interband paths can carry imaginary traces and hence an odd-order finite part. (d) The map $\boldsymbol{n}(\boldsymbol{k})$ to the Bloch sphere relates these traces to quantum geometry: squared tangent lengths encode the quantum metric, and oriented areas encode Berry curvature.

Figure 2. Interband finite part across fillings, temperatures, and relaxation prescriptions. Results for equation (10) with $(m, \lambda_1, \lambda_2) = (1.2, 0.5, 0.35)$. (a) $\sigma^{(3),[0]}_{yxxx}$ versus filling at $T = 0.1t$: the bath result from equation (8) (solid) and finite-rate extrapolations (open circles). Bars quantify fit sensitivity: the largest intercept change across $q = 1, 2, 3$ fitting bases and three nested rate windows at fixed fitted pole order $N = 4$ (Methods and Supplementary Information, Sec. VI.A). They are not statistical error bars. The grey line is the zero scalar-reference finite part. Dash-dotted and dotted curves show relaxation-time approximation (RTA) results for an order-dependent rate N/τ (response order N) and a uniform rate $1/\tau$, respectively, using the same Hamiltonian. All curves use symmetric kernel units $3!\bar{\sigma}$. The vertical line marks the lower-band van Hove singularity (vHS) at $-1.38t$. (b) Bath result versus temperature at $\mu = -t$, compared with finite-rate extrapolations.

Figure 3. Momentum-space decomposition of the third-order finite part. Momentum-resolved third-order finite part for equation (10) at $\mu = -t$ and $T = 0.1t$: (a) total response; (b) curvature–metric group; (c) Berry curvature multiplied by the squared gap gradient; (d) all remaining derivative terms, including Av^y, Ωv^{xx}, uB, and $\mathcal{E}$ in the notation of Supplementary Information, Sec. IV.D. The numbers below the maps are Brillouin zone means in symmetric kernel units. Panels (a), (b), and (d) share a color scale; panel (c) uses its own scale. Red and blue denote positive and negative contributions, respectively.

Figure 4. Conductivity scaling intercept and microscopic finite part. Results for equation (10) at $\mu = -t$ and $T = 0.1t$. Panel (b) uses symmetric kernel units. (a) $\Gamma\sigma_{xx}$ from the finite-rate Kubo bubble (points) and the expansion $D_x + b\Gamma^2 + c\Gamma^3$ (line). (b) The total third-order kernel F after subtracting its divergent Laurent terms (circles) or its positive-power terms in σ_{xx} (squares). The corresponding limits are the microscopic finite part $\sigma^{(3),[0]}_{yxxx} = 0.109$ and the conductivity scaling intercept $C_0^{(\sigma)} = 0.194$. Their difference is fixed by equation (11); the finite-rate data and longitudinal coefficients are detailed in Supplementary Information, Sec. VI.C and Appendix B. Dashed horizontal lines mark the two limiting constants.

Supplementary Files

This is a list of supplementary files associated with this preprint. Click to download.

- SupplementaryInformationLaTeX.zip
- SupplementaryData1.zip